PAPER

Check for updates

Identifying high-efficiency oxygen evolution electrocatalysts from Co–Ni–Cu based selenides through combinatorial electrodeposition†

Xi Cao, [ID] [a] Emily Johnson[b] and Manashi Nath [ID] *[a]

Water splitting has been widely considered to be an efficient way to generate sustainable and renewable energy resources in fuel cells, metal–air batteries and other energy conversion devices. Exploring efficient electrocatalysts to expedite the anodic oxygen evolution reaction (OER) is a crucial task that needs to be addressed in order to boost the practical application of water splitting. Intensive efforts have been devoted to develop mixed transition metal based chalcogenides as effective OER electrocatalysts. Herein, we have reported synthesis of a series of mixed metal selenides containing Co, Ni and Cu employing combinatorial electrodeposition, and systematically investigated how the transition metal doping affects the OER catalytic activity in alkaline medium. Energy dispersive spectroscopy (EDS) was performed to detect the elemental compositions and confirm the feasibility of compositional control of 66 metal selenide thin films. It was observed that the OER catalytic activity is sensitive to the concentration of Cu in the catalysts, and the catalyst activity tended to increase with increasing Cu concentration. However, increasing the Cu concentration beyond a certain limit led to decrease in catalytic efficiency, and copper selenide by itself, although catalytically active, showed higher onset potential and overpotential for OER compared to the ternary and quaternary mixed metal selenides. Interestingly, the best quaternary composition $(Co_{0.21}Ni_{0.25}Cu_{0.54})_3Se_2$ showed similar crystal structure as its parent compound of Cu_3Se_2 with slight decrease in lattice spacings of (101) and (210) lattice planes (0.0222 Å and 0.0148 Å, respectively) evident from the powder X-ray diffraction pattern. $(Co_{0.21}Ni_{0.25}Cu_{0.54})_3Se_2$ thin film exhibited excellent OER catalytic activity and required an overpotential of 272 mV to reach a current density of 10 mA cm^{-2}, which is 54 mV lower than Cu_3Se_2, indicating a synergistic effect of transition metal doping in enhancing catalytic activity.

Introduction

The growing demand for energy and increasing concerns about the environmental pollution from burning fossil fuels have led to an intense interest in discovering alternative sources of energy from sustainable resources.[1,2] In that regard, hydrogen (H_2) has been widely considered as a promising alternative energy substitute for fossil fuels resulting from its high energy density and reduced environmental impacts.[3–5] The traditional way to produce H_2 is through natural gas reforming in industry which results in low purity and high cost.[6] Water electrolysis assisted by electricity or sunlight is an emerging and efficient technology to generate high purity H_2 on demand, where H_2 evolution reaction (HER) happens at the cathode and O_2 evolution reaction (OER) takes place at the anode.[3,7,8] However, water electrolysis to produce H_2 for large-scale application, unfortunately, has been highly hindered due to the kinetically sluggish OER resulting from the four-electron transfer process involved in the reaction.[9,10] An effective electrocatalyst is needed to lower the activation barrier and facilitate kinetics of the OER process and therefore increase the practical feasibility of large-scale water splitting reaction. During the past several decades, large number of research efforts have led to the discovery of robust, stable, and effective OER electrocatalysts that can reduce the overpotential for water oxidation and hence increase the energy efficiency.[2,11–14] Among these, precious metal based OER catalysts, such as IrO_2 and RuO_2, show excellent catalytic activity and high durability in the alkaline medium, nevertheless, these catalysts suffer from scarcity on earth's surface, and are consequently too expensive for bulk utilization in industry.[15,16] Recently, intensive research efforts have been concentrated on the investigation of earth abundant transition-metal-based materials as high efficiency OER catalysts,

[a]Department of Chemistry, Missouri University of Science & Technology, Rolla, Missouri 65409, USA. E-mail: nathm@mst.edu

[b]Department of Chemical and Biochemical Engineering, Missouri University of Science & Technology, Rolla, Missouri 65409, USA

† Electronic supplementary information (ESI) available: Supporting information includes XRD figures, LSV plots, summary table, EDS table before and after chronoamperometry, XPS comparison spectra and crystal structures. See DOI: 10.1039/c9ta00863b

This journal is © The Royal Society of Chemistry 2019

J. Mater. Chem. A, 2019, 7, 9877–9889 | 9877

comprising elements such as Ni, Fe, Co, and Mn.[17–23] Several factors were proposed to relate the high OER catalytic activity to the transition-metal-based compositions: (i) the ability of catalytically active 3d metal sites to easily switch between different oxidation states ($Ni^{2+/3+}$, $Co^{2+/3+}$ *etc.*) without hindrance under application of small electric bias,[7,24] (ii) the number of electrons occupying the e_g orbitals of the 3d metal ions on the surface which will likely affect the bond strength between catalytic sites and hydroxyl species and even influencing the surface oxygen binding energy,[25–27] therefore reducing the thermodynamic overpotential of the OER process. Besides transition metal cations, anions can also influence the OER catalytic activity as well by changing covalency of the metal–ligand bond which leads to tuning of the redox potential of the catalytically active transition metal center.[28] Recently, transition-metal-based chalcogenides such as sulfides,[29–31] phosphides[32–34] and selenides[35–38] exhibited improved efficiency in comparison to the corresponding oxides and (oxy)hydroxides[13,39–43] in alkaline medium. Among the chalcogenides, selenides and tellurides have been reported to have a better catalytic activity since the smaller electronegativity of selenium/tellurium leads to an increased covalency in the metal–chalcogen bond which facilitates the catalyst activation and onset of OER reaction by lowering the redox potential of the catalytic site.[44,45] Interestingly, incorporation of dopant elements into pure transition-metal-based catalysts has been observed to dramatically enhance the OER catalytic activity in both oxides and chalcogenides.[13,27,30,46–48] This observation is most likely attributed to several factors including increasing the amount of active sites among the catalytic systems; tuning of the electron density over the catalytic centers through inductive effect of the neighboring dopant atoms, as well as tuning the hydroxyl (OH^-) adsorption energy at the catalytic center to an optimal energy level, which leads to lowering of the potential to initiate the multistep OER process.[49–51] Researchers have thus devoted considerable efforts to investigate efficient mixed-transition-metal-based OER catalysts. However, such work exhibiting systematic compositional and/or stoichiometric variation of multinary catalyst compositions are limited.[52–54] It is necessary to develop an efficient and systematic screening method to explore the compositional space for multinary catalytic systems and discover non-stoichiometric compositions which might be missed in the targeted synthesis technique without prior knowledge. Smith *et al.* for example, has carried out a systematic study of the OER activity trend of amorphous oxides containing Ni, Fe and Co and identified the best composition as α-$Fe_{20}Ni_{80}$ oxide, while A. Shinde *et al.* showed the improved photocatalytic activity of $Fe_{(0.4–0.6)}Ce_{(0.6–0.4)}O_x$ modified $BiVO_4$ photoanode created through high-throughput inkjet printing.[55,56] Our group has recently reported a more efficient and economical method – combinatorial electrodeposition – to systematically investigate the Ni–Fe–Co trigonal phase diagram and identified the quaternary selenide $(Ni_{0.25}Fe_{0.68}Co_{0.07})_3Se_4$ as an efficient OER electrocatalyst with low overpotential of 230 mV at 10 mA cm^{-2} as well as an excellent durability in alkaline medium.[57] Given the fact that Ni, Fe, Co and Mn based compounds have been intensively explored as active OER catalysts in recent years,

researchers have started expanding their investigation of other transition metals with high d-electron count, such as copper. While, copper is one of the most earth-abundant and low-cost elements with high electrical conductivity, however, Cu-based compounds have been less explored as water oxidation electrocatalysts. Thomas J. Meyer's group has studied simple Cu(II) ions and homogeneous Cu(II) polypeptide complex as OER catalysts in buffer solution.[58,59] Apart from such homogeneous catalysts, Cu-based electrocatalysts (such as CuO, $CuFe_2O_4$, $CuCo_2O_4$ and $CuCo_2S_4$ *etc.*) have been studied and exhibited moderate OER catalytic activities.[60–64] Cu with its high d-electron density can modulate the electron density around the other transition metal centers through d–d band formation, which consequently will affect the OH adsorption on the catalytically active site and the reaction kinetics. Cu also imparts better conductivity to the catalyst composite which will lead to better charge transport through the catalytic film and hence better OER catalytic activity. Recently, we have also showed that Cu_2Se nanoparticles and electrodeposited films exhibited an improved catalytic activity in comparison of Cu-based oxides and complexes in alkaline medium.[65] However, the effect of Cu doping in OER active catalyst composition has been hitherto unknown. In this article, we have reported for the first time, a systematic study of Co–Ni–Cu selenides through combinatorial electrodeposition to investigate the effect of transition metal doping and have identified the optimal OER catalyst in this group. Most of the quaternary metal selenides crystallized in the Cu_3Se_2 (umangite) structure type, which also shows excellent OER catalytic activity by itself, with a low overpotential of 326 mV at 10 mA cm^{-2}, and has been reported for the first time in this article. Through detailed electrochemical measurements it was observed that in this mixed metal group, the catalytic activity in quaternary composition is better than ternary as well as binary selenides. Moreover, it was also observed that the catalytic activity was sensitive to the concentration of Cu in the catalyst. The best performing quaternary composition was identified as $(Co_{0.21}Ni_{0.25}Cu_{0.54})_3Se_2$, requiring an overpotential of 272 mV to reach 10 mA cm^{-2}. Powder X-ray diffraction (pxrd) pattern confirmed that $(Co_{0.21}Ni_{0.25}Cu_{0.54})_3Se_2$ showed the same crystal structure of Cu_3Se_2 with slight decrease in lattice spacing (0.0222 Å and 0.0148 Å for (101) and (210) plane, respectively), indicating that small amount Ni and Co dopants led to only small change of the lattice parameters of Cu_3Se_2.

Experimental

Materials

Nickel(II) sulfate [$NiSO_4 \cdot 6H_2O$, 99%], cobalt(II) sulfate [$CoSO_4 \cdot 7H_2O$, 99%], copper(II) sulfate [$CuSO_4 \cdot 5H_2O$, 99%], selenium dioxide [SeO_2], lithium chloride [LiCl, 99%], potassium hydroxide [KOH, 85%], were purchased from Fisher Scientific. All the chemicals were used as received without further purification. Deionized (DI) water (18 MΩ cm^{-1}) was used to prepare all the electrolytes. Au-coated glass substrates were purchased from Deposition Research Lab Incorporated (DRLI), Lebanon, Missouri.

9878 | *J. Mater. Chem. A*, 2019, 7, 9877–9889

This journal is © The Royal Society of Chemistry 2019

Combinatorial electrodeposition of thin films

Electrodeposition of a series of ternary (or quaternary) thin films by exploring the trigonal phase diagram, as shown in Fig. S1,† was carried out following method similar to the one reported previously from our group.[57] The electrolytes containing 10 mM $NiSO_4 \cdot 6H_2O$ (or $CoSO_4 \cdot 7H_2O$, $CuSO_4 \cdot 5H_2O$), 10 mM SeO_2 and 25 mM LiCl were freshly prepared and purged with N_2 for 30 min before electrodeposition. Prior to electrodeposition, the Au-coated glass substrates were carefully cleaned in micro-90, followed by isopropanol and rinsed with deionized water. Then all the cleaned substrates were confined with Teflon tape containing a hole of fixed dimensions, to make sure all the thin films had the same geometric area. All the electrodeposition experiments were carried out using an IviumStat potentiostat, with an electrolyte volume of 50 mL in a three-electrode setup consisting of an Ag|AgCl (KCl saturated) reference electrode, glassy carbon (GC) counter electrode, and Au-coated glass as working electrode. Thin films were formed by applying a potential of −0.85 V vs. Ag|AgCl (KCl saturated) for 300 s at room temperature. The deposition potential was selected by analyzing the film composition over a range of deposition potentials as listed in Table S1† which revealed that −0.85 V vs. Ag|AgCl was the optimal potential to achieve compositional control and stability of the deposited film.

Characterization

The as-electrodeposited thin films were characterized through powder X-ray diffraction (pxrd) using Philips X-Pert diffractometer and Cu Kα (1.5418 Å) radiation. Because the product was a very thin layer formed on the substrate, the pxrd was collected at grazing angle incidence in thin film geometry (GI mode with Göbel mirrors). X-ray photoelectron spectroscopy (XPS) measurements of the catalysts were performed using a KRATOS AXIS 165 X-ray Photoelectron Spectrometer with the monochromatic Al X-ray source. All XPS analyses were performed on the pristine films without any sputtering. Scanning electron microscopy (SEM) was carried out to examine the morphology of film by the FEI Helios NanoLab 600 FIB/FESEM at an accelerating voltage of 15 kV. Energy dispersive spectroscopy (EDS) analysis was also obtained from the same SEM microscope. In this work, EDS analysis was performed on three to five different regions on each sample surface to calculate the average elemental ratio. The molecular formula of each compound is written as $(Co_xNi_yCu_z)Se_n$, where x, y, z are the relative atomic ratios obtained from EDS analysis ($x + y + z = 1$) while n is the amount of Se relative to the total metal.

Electrochemical measurements

The electrocatalytic efficiencies were measured in a three-electrode electrochemical cell with an IviumStat potentiostat. The OER catalytic activity was measured by linear sweep voltammetry (LSV) while the stability was studied by constant potential chronoamperometry in N_2-saturated 1.0 M KOH solution at room temperature. All LSV plots shown in this work were iR corrected. The deposited thin films served as the working electrode, GC as the counter electrode and Ag|AgCl (KCl saturated) as the reference electrode. All experimentally measured potentials vs. Ag|AgCl (KCl saturated) were converted to the reversible hydrogen electrode (RHE) using the Nernst equation shown as eqn (1).

$$E_{RHE} = E_{Ag|AgCl} + 0.059pH + E^o_{Ag|AgCl} \qquad (1)$$

Here, the standard potential of Ag|AgCl (KCl saturated) at 25.1 °C is 0.197 V vs. RHE.

Calculation of Tafel slope

The electrochemical kinetics of the $(Co_xNi_yCu_z)Se_n$ catalysts towards OER relating the overpotential η with the current density j has been carried out by calculating the Tafel slopes using the eqn (2).

$$\eta = a + \frac{2.3RT}{\alpha nF}\log(j) \qquad (2)$$

where η is the overpotential, j is the current density and the other symbols have their usual meaning. The Tafel slope is given by $2.3RT/\alpha nF$. The Tafel slopes were calculated from LSV with a scan rate (2 mV s^{-1}) in non-stirred N_2-saturated 1.0 M KOH solution.

Electrochemically active surface area (ECSA)

The electrochemically active surface area (ECSA) of the catalyst was measured from the electrochemical double layer capacitance as described in previous reports.[57] Cyclic voltammograms (CVs) with various scan rates were used to measure the double layer charging current in a non-faradaic region. The double-layer current (i_{DL}) occurring in non-faradaic region can be assumed to be from the response of double-layer charging instead of chemical reaction or charge transfer. The electrochemical double-layer capacitance (C_{DL}) can be estimated from the plot of cathodic and anodic double-layer current i_{DL} versus scan rates (ν) as shown in eqn (3). The C_{DL} was simply determined from the average of the cathodic and anodic slopes. ECSA can be calculated by eqn (4), by dividing the double-layer capacitance (C_{DL}) by the specific capacitance (C_s), where double-layer capacitance (C_{DL}) is in unit of mF.

$$i_{DL} = C_{DL} \times \nu \qquad (3)$$

$$ECSA = C_{DL}/C_s \qquad (4)$$

In our study of surface area, the specific capacitance (C_s) was assumed to be 0.040 mF cm^{-2} based on reported value.[35,66] Roughness factor (RF) is calculated by dividing the ECSA with geometric area 0.07 cm^2.

Results and discussion

Structural and elemental compositions of electrodeposited thin films

The binary, ternary and quaternary mixed metal selenide films were deposited through combinatorial electrodeposition exploring a trigonal phase space of Ni–Cu–Co with a fixed

This journal is © The Royal Society of Chemistry 2019

J. Mater. Chem. A, 2019, **7**, 9877–9889 | **9879**

amount of Se, as shown in Fig. S1.† In this trigonal phase diagram, the vertices represent binary selenides (CoSe, NiSe and Cu_3Se_2), while the axes of the triangle refer to the ternary selenides $Co_xCu_ySe_n$, $Ni_xCo_ySe_n$ and $Ni_xCu_ySe_n$, respectively. The interior of this triangle represents the quaternary mixed-metal selenide ($Co_xNi_yCu_zSe_n$). The compositions of three binary selenides were confirmed using powder X-ray diffraction (pxrd) as shown in Fig. S2,† which revealed that electrodeposited copper selenide, (Cu_3Se_2, shown in Fig. S2a†) and nickel selenide (NiSe, shown in Fig. S2b†) were crystalline and the diffraction peaks matched perfectly with the standard diffraction pattern of Cu_3Se_2 (PDF # 00-047-1745) and NiSe (PDF # 01-075-0610), respectively. However, no clear diffraction peaks corresponding to cobalt selenide could be observed in the pxrd pattern as shown in Fig. S2c† (the observed diffraction peaks correspond to Au from the Au-glass substrate), indicating that the electrodeposited cobalt selenide is predominantly amorphous. The elemental compositions of three binary catalysts were further analyzed using energy dispersive spectroscopy (EDS) as shown in Table S2.† Since the pxrd patterns were generally not very well-defined in electrodeposited films,[37] the composition of the binary selenides were ascertained by using both EDS and pxrd analyses as applicable. It can be seen that the three as-prepared binary catalysts were composed of Cu, Ni or Co and Se with approximate atomic ratio of 3 : 2 (Cu : Se), 1 : 1 (Ni : Se) and 1 : 1 (Co : Se) respectively, which is consistent with the pxrd characterizations, and three binaries has been denoted as Cu_3Se_2, CoSe and NiSe, respectively. Similarly, molecular formulae of all ternaries and quaternaries identified in this study were ascertained in the same way by using the EDS elemental ratio and have been listed in Table S3.† It can be also observed in Table S2† that the relative atomic percentage of an element increased (or decreased) with increasing (or decreasing) amounts of the corresponding metal precursor in the electrolytic bath, indicating the feasibility of compositional control through such a combinatorial electrodeposition.

Electrochemical characterization

The linear sweep voltammetry (LSV) was performed in N_2-saturated 1.0 M KOH solution at a scan rate of 10 mV s^{-1} to study the OER catalytic activity. Two kinetic parameters were selected to benchmark the electrocatalytic performance: (i) onset overpotential (onset η) and (ii) overpotential required to reach a current density 10 mA cm^{-2} (η at 10 mA cm^{-2}).[66,67] These two kinetic parameters for all electrodeposited selenides along with their corresponding EDS atomic ratios have been summarized and shown in Table S2.† Fig. S3† shows the OER polarization curves measured in N_2-saturated 1.0 M KOH for three binary selenides. The catalytic activity trend for three binaries was CoSe > Cu_3Se_2 > NiSe. The LSV plots of the Co–Cu selenides group, presented in Fig. 1a, indicate they are indeed highly active towards OER. It can be observed that ($Co_{0.40}Cu_{0.60})_3Se_2$ showed the best catalytic activity in this group with the lowest onset overpotential of 257 mV and overpotential of 278 mV to reach a current density of 10 mA cm^{-2}. For the Ni–Co selenides group shown in Fig. 1b, it was observed that the

catalytic activity improved with increasing the amount of Co and ($Ni_{0.51}Co_{0.49}$)Se exhibited the best activity with an onset overpotential of 259 mV and overpotential of 289 mV at 10 mA cm^{-2}. The OER performance of Ni–Cu selenides group in Fig. 1c showed that decreasing the amount of Cu boosted the OER activity, wherein the best composition ($Ni_{0.77}Cu_{0.23})_3Se_2$ in this group required an onset overpotential of 268 mV and overpotential of 299 mV to achieve 10 mA cm^{-2}. It should be noted here that some pre-oxidation peaks were observed in the OER LSV curves as shown in Fig. 1a–d. These peaks have been widely observed in Ni- and Co-based electrocatalysts, resulting from the transition metal's oxidation state changing in the catalyst during application of a high anodic potential.[13,68–70] In Fig. 1, peaks around 1.15 V vs. RHE correspond to Co^{2+} to Co^{3+} conversion, while those around 1.35 V vs. RHE are due to Ni^{2+} to Ni^{3+} oxidation.[68,69] These pre-oxidation peaks are also considered to be catalyst activation steps, especially for Ni-based catalysts, where Ni^{3+} is the actual catalytically active center. Interestingly, more predominant peaks of Co^{2+} to Co^{3+} conversion can be found in Fig. 1b when the Co content is higher in the catalysts, while there's no specific relationship of the intensity of Ni pre-oxidation peak with respect to the Ni amount in catalyst, presumably due to the fact that Ni can coexist in the +2 and +3 oxidation states in as-synthesized catalysts depending on the crystal structure and stoichiometry.[71] Fig. 1d shows the comparative plots of the best performing ternary selenide compositions in each group compared with the three binary selenides. It can be seen that 40% of Co doped into Cu_3Se_2 enhanced the OER catalytic activity with a decrease of onset overpotential and overpotential at 10 mA cm^{-2} by 25 mV and 48 mV, respectively. The onset overpotential drop indicated an improvement in the intrinsic property of ($Co_{0.40}Cu_{0.60})_3Se_2$ compared to Cu_3Se_2. Similarly, 49% Co doped into NiSe decreased the onset overpotential and overpotential at 10 mA cm^{-2} by 41 mV and 46 mV, respectively. However, there was no significant improvement of OER activity with 23% of Cu doped into NiSe. It should be mentioned that the enhancement in catalytic activity by introducing transition metal dopants into the lattice may be attributed to the extensive electron delocalization occurring through d–d orbital interactions between the catalytic centers, leading to modulation of electron density near the catalytic center, thereby, facilitating catalyst activation and charge transfer within the catalyst. For instance, the catalytic activity of Ni- and Co-based electrocatalysts can be dramatically improved with the introduction of Fe.[13,72–74] To compare the electrocatalytic properties of the quaternary selenides as a function of compositional variation, contour plots as shown in Fig. 2 were constructed based on the relative atomic ratio obtained through EDS and the two kinetic parameters (onset η and η at 10 mA cm^{-2}) as given in Table S2.† The contour plot provided in Fig. 2a shows the trend of OER onset overpotential, while the trend of overpotential at the current density of 10 mA cm^{-2} as a function of film composition has been shown in Fig. 2b. As can be seen in Fig. 2a, an area inside of the trigonal plot (quaternary phases) and adjacent to the Co axis (Co–Cu selenides) showed lower overpotential indicating the best catalytic activity within the Ni–Co–Cu ternary phase space, while
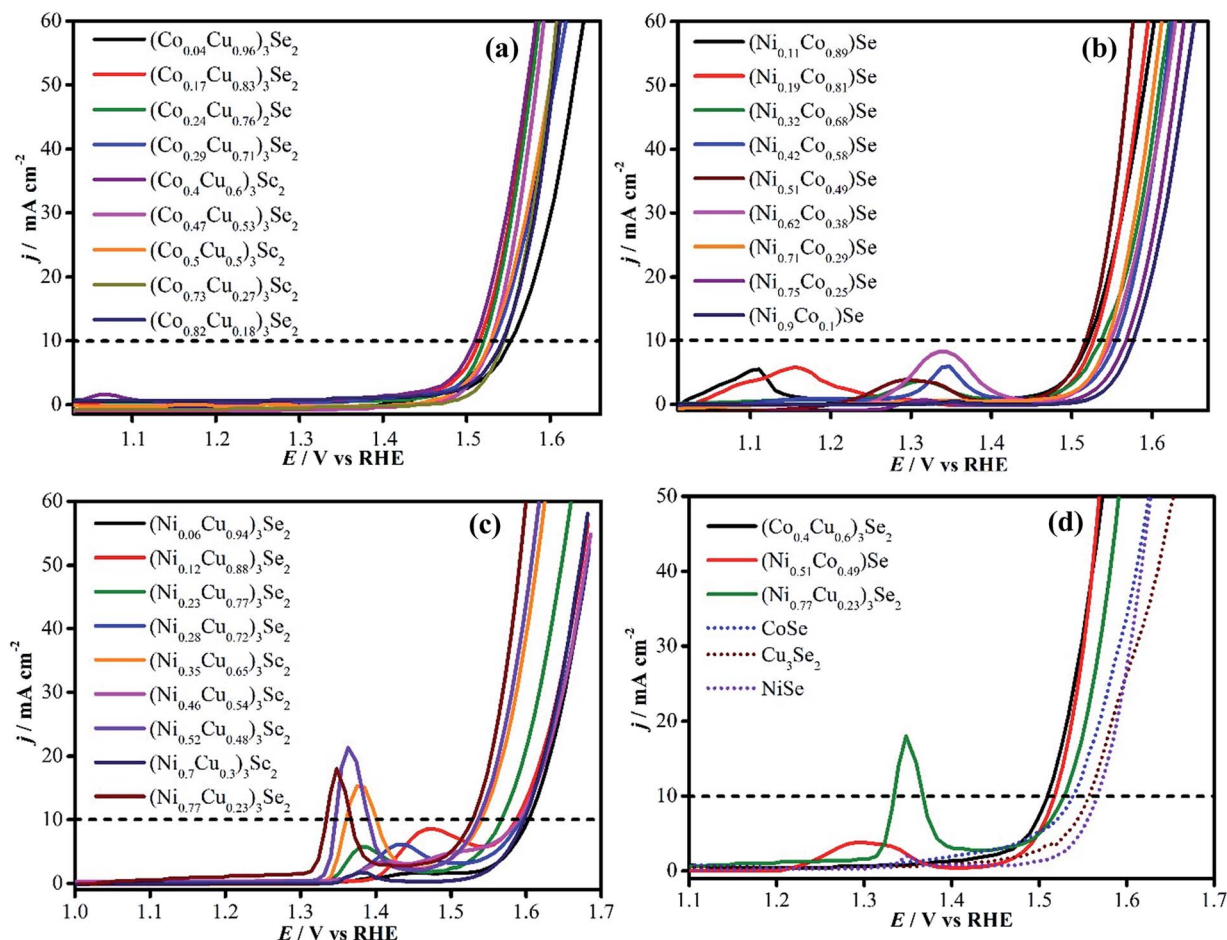
9880 | J. Mater. Chem. A, 2019, 7, 9877–9889

This journal is © The Royal Society of Chemistry 2019

Fig. 1   Linear sweep voltammetries (LSVs) of ternary metal selenides along the edges of the trigonal phase diagram. (a) Co–Cu group (b) Ni–Co group (c) Ni–Cu group. (d) Comparison of the best performing ternary composition (solid line) from each group along with the binary compositions (dotted line). The dashed black line in each panel marks the current density at 10 mA cm^{-2}.
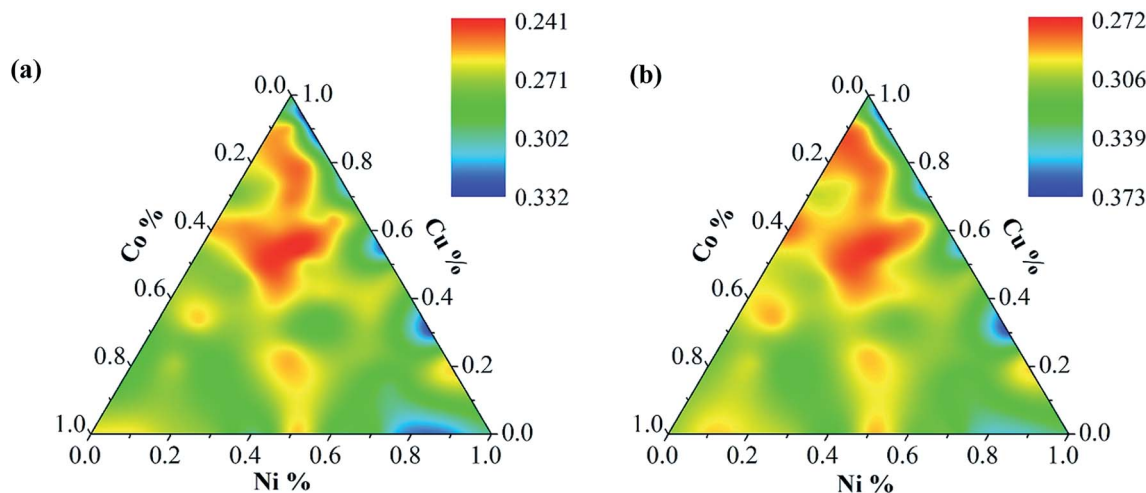

Fig. 2   Contour plots of onset overpotential η (in units of V) (a) and (b) overpotential η (in units of V) at the current density of 10 mA cm^{-2} for the entire Co–Ni–Cu trigonal phase space. The color gradient corresponds to the overpotential measured in volts.

the regions next to the Ni (Ni–Co selenides) and Cu axes (Ni–Cu selenides) exhibited less efficient catalytic activity. Typically, quaternary films showed a lower onset η when the concentration of copper was kept relatively higher than that of cobalt or nickel, where Cu was about 40–90%, Co was around 10–40% while Ni was at 0–30%. In the absence of nickel, Co–Cu

axis produced a lower onset η, specially, when copper amount was larger than 40%. Similar trends were also observed in Fig. 2b. The trends indicated the mixed metal selenides were more likely to have optimal catalytic performance in the presence of 40–90% Cu, indicating copper doping had a remarkable positive effect on the OER catalytic activity. This observation further confirmed that transition-metal doping can optimize the intrinsic property of electrocatalysts and improve the catalytic activity by dramatically reducing the onset η and η at 10 mA cm^{-2}.

The OER LSV plots of seven quaternary compounds with best catalytic performance in N$_2$-saturated 1.0 M KOH at a scan rate of 10 mV s^{-1} has been presented in Fig. 3a. These compositions can be represented as, $(Co_{0.08}Ni_{0.28}Cu_{0.63})_3Se_2$, $(Co_{0.15}Ni_{0.15}Cu_{0.7})_3Se_2$, $(Co_{0.15}Ni_{0.26}Cu_{0.59})_3Se_2$, $(Co_{0.21}Ni_{0.25}Cu_{0.54})_3Se_2$, $(Co_{0.31}Ni_{0.08}Cu_{0.61})_3Se_2$, $(Co_{0.31}Ni_{0.23}Cu_{0.46})_3Se_2$ and $(Co_{0.36}Ni_{0.07}Cu_{0.57})_3Se_2$. It was interesting to note that for the quaternary selenides, the metal to selenium ratio was obtained as 3 : 2 and that all these phases could be formulated as M_3Se_2 ($M =$ total metal concentration). As can be seen, the onset η of $(Co_{0.08}Ni_{0.28}Cu_{0.63})_3Se_2$ was 256 mV and it required η of 287 mV to reach a current density of 10 mA cm^{-2}. The onset η of $(Co_{0.15}Ni_{0.15}Cu_{0.7})_3Se_2$ was 251 mV and it yielded a current density of 10 mA cm^{-2} at a η of 283 mV. The onset η of $(Co_{0.15}Ni_{0.26}Cu_{0.59})_3Se_2$ was 246 mV and η at 10 mA cm^{-2} was 278 mV. The onset η and η at 10 mA cm^{-2} of $(Co_{0.31}Ni_{0.08}Cu_{0.61})_3Se_2$ were 254 mV and 282 mV, respectively. The onset η of $(Co_{0.31}Ni_{0.23}Cu_{0.46})_3Se_2$ was 248 mV and it needed a η of 280 mV to achieve a current density of 10 mA cm^{-2}. The onset η of $(Co_{0.36}Ni_{0.07}Cu_{0.57})_3Se_2$ was 257 mV and 284 mV at 10 mA cm^{-2}. $(Co_{0.21}Ni_{0.25}Cu_{0.54})_3Se_2$ exhibited the best catalytic activity within this group with an onset η of 241 mV and a η of 272 mV to reach 10 mA cm^{-2}. SEM images of several of these quaternary selenides $(Co_{0.08}Ni_{0.28}Cu_{0.63})_3Se_2$, $(Co_{0.31}Ni_{0.23}Cu_{0.46})_3Se_2$, $(Co_{0.15}Ni_{0.26}Cu_{0.59})_3Se_2$ and $(Co_{0.21}Ni_{0.25}Cu_{0.54})_3Se_2$ has been shown in Fig. S4† exhibiting a nano-flake like geometry for most of these films. The SEM results further suggested that the morphology did not change drastically with respect to the elemental composition.

Tafel slope is an important parameter to evaluate the kinetics of an electrocatalyst. Therefore, the Tafel slopes of all catalysts reported in this work were calculated and shown in Table S2.† The Tafel plots (η *vs.* $\log j$) of the seven quaternary selenides were plotted and the Tafel slopes have been shown in Fig. 3b. The Tafel slopes were 74.3, 71.3, 93.9, 53.3, 57.0, 78.9 and 67.5 mV dec^{-1} for $(Co_{0.08}Ni_{0.28}Cu_{0.63})_3Se_2$, $(Co_{0.15}Ni_{0.15}Cu_{0.7})_3Se_2$, $(Co_{0.15}Ni_{0.26}Cu_{0.59})_3Se_2$, $(Co_{0.21}Ni_{0.25}Cu_{0.54})_3Se_2$, $(Co_{0.31}Ni_{0.08}Cu_{0.61})_3Se_2$, $(Co_{0.31}Ni_{0.23}Cu_{0.46})_3Se_2$ and $(Co_{0.36}Ni_{0.07}Cu_{0.57})_3Se_2$, respectively. As can be seen, they all showed small Tafel slopes suggesting that they were all kinetically favorable and the second and third step in OER were likely to be the rate-determining steps.[66,75] Based on these observations, it is obvious that the best catalytic activity was exhibited by the quaternary compound of composition $(Co_{0.21}Ni_{0.25}Cu_{0.54})_3Se_2$ with the lowest overpotentials and Tafel slopes, which is significantly more efficient than other well-known precious metal based catalysts, such as RuO$_x$.[15]

The quaternary composition, $(Co_{0.21}Ni_{0.25}Cu_{0.54})_3Se_2$ thin film showing the best catalytic activity, was further characterized through pxrd and other analytical techniques to study its composition and morphology. The pxrd pattern of the as-deposited thin film was compared with the as-deposited Cu$_3$Se$_2$ film as shown in Fig. 4. As can be seen, all the peaks of as-deposited Cu$_3$Se$_2$ perfectly matched with the reference XRD pattern of Cu$_3$Se$_2$ (PDF # 00-047-1745), suggesting the high crystallinity and purity of the thin film. Interestingly, $(Co_{0.21}Ni_{0.25}Cu_{0.54})_3Se_2$ thin film showed similar pxrd pattern as that of standard Cu$_3$Se$_2$ (PDF # 00-047-1745) with some shift of the diffraction peaks which indicated that 21% of Co and 25% Ni were actually doped inside the parent compound Cu$_3$Se$_2$ lattice leading to similar crystal structure with slight volume change of the crystal lattice. For example, the peaks around a two-theta of 25° showed a shift of 0.16 degree towards higher-angle side, indicating slight change in the lattice parameters on heteroatom doping in the parent Cu$_3$Se$_2$ lattice. Peaks observed at 25.0°, 31.2°, 39.8°, 49.8°, and 51.3° were indexed to the (101), (210), (220), (311) and (202) lattice planes, respectively. The *d*-
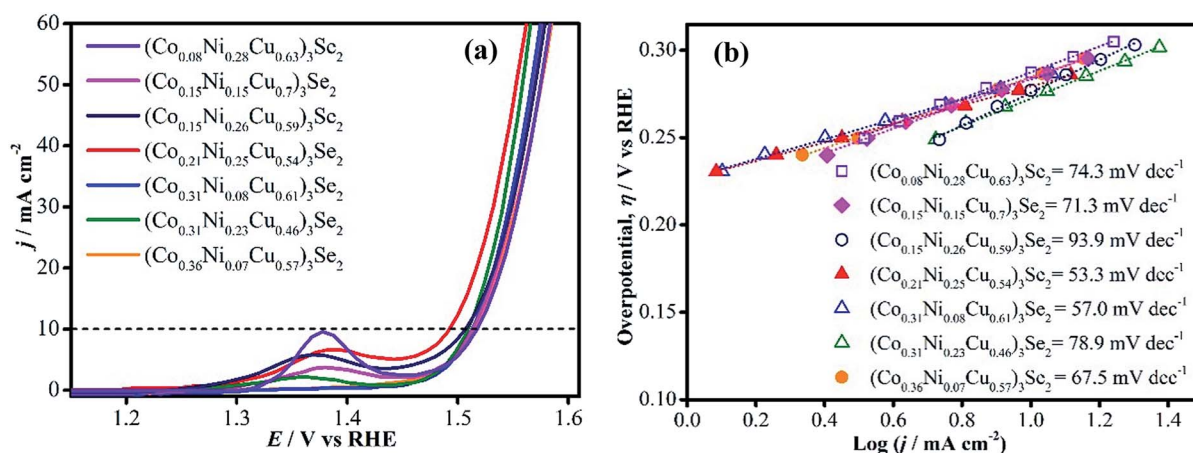

Fig. 3 (a) LSVs of the seven best quaternary compositions measured in N$_2$-saturated 1.0 M KOH solution at a scan rate of 10 mV s^{-1}. (b) Tafel plots of the catalysts.
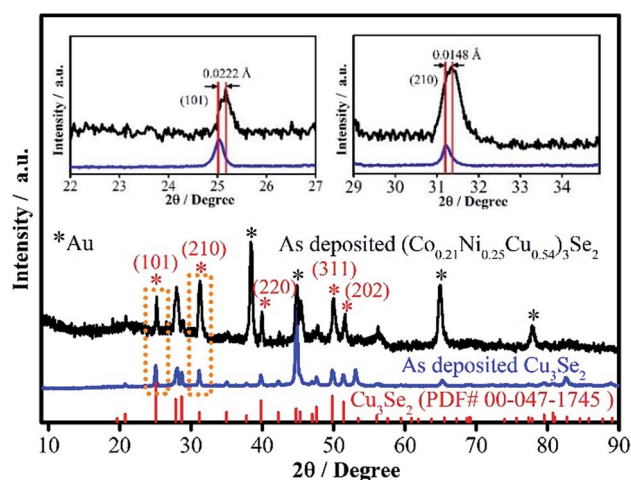
9882 | *J. Mater. Chem. A*, 2019, **7**, 9877–9889

This journal is © The Royal Society of Chemistry 2019

Fig. 4 XRD patterns of as-deposited $(Co_{0.21}Ni_{0.25}Cu_{0.54})_3Se_2$ (black line) and Cu_3Se_2 (blue line) thin films on Au coated glass along with reference Cu_3Se_2 (PDF # 00-047-1745). The insets are the comparisons of zoomed-in (101) and (210) peaks of $(Co_{0.21}Ni_{0.25}Cu_{0.54})_3Se_2$ (black line) compared with those of Cu_3Se_2 (blue line).

spacing of two dominant planes of (101) and (210) in $(Co_{0.21}Ni_{0.25}Cu_{0.54})_3Se_2$ were compared with that of Cu_3Se_2 which showed decreases of 0.0222 Å (0.62%) and 0.0148 Å (0.52%) for (101) and (210) lattice spacings respectively relative to the parent compound Cu_3Se_2 as inserted in Fig. 4.[76] The size of crystalline domains of $(Co_{0.21}Ni_{0.25}Cu_{0.54})_3Se_2$ was estimated to be 3–4 nm from the pxrd pattern using the Scherrer equation,[77] indicating the electrodeposited film was actually polycrystalline.

To understand the trend of catalytic activity with respect to transition metal doping, the LSV curve of the best performing quaternary $(Co_{0.21}Ni_{0.25}Cu_{0.54})_3Se_2$ was compared with those of Cu_3Se_2, NiSe and CoSe in N_2-saturated 1.0 M KOH collected at a scan rate of 10 mV s^{-1} as shown in Fig. 5a. As can be seen, to reach a current density of 10 mA cm^{-2}, the overpotentials required for CoSe, Cu_3Se_2 and NiSe were 308, 326 and 335 mV, respectively. The onset overpotentials of CoSe, Cu_3Se_2 and NiSe were 262, 282 and 300 mV, respectively. CoSe showed the best catalytic activity among binary selenides. With Ni and Co doped into Cu_3Se_2, the onset overpotential of $(Co_{0.21}Ni_{0.25}Cu_{0.54})_3Se_2$ significantly dropped to 241 mV and it yielded an overpotential of only 272 mV to achieve a current density of 10 mA cm^{-2}. The Tafel slope for $(Co_{0.21}Ni_{0.25}Cu_{0.54})_3Se_2$ (53.3 mV dec^{-1}) was lower than that of NiSe (66.2 mV dec^{-1}), Cu_3Se_2 (82.9 mV dec^{-1}) and CoSe (177.4 mV dec^{-1}) as shown in Table S2,† indicating the quaternary selenide is kinetically more favorable than the binaries. A comparison of LSV curves of $(Co_{0.21}Ni_{0.25}Cu_{0.54})_3Se_2$ with three best performance ternary selenides $(Co_{0.40}Cu_{0.60})_3Se_2$, $(Ni_{0.51}Co_{0.49})Se$ and $(Ni_{0.77}Cu_{0.23})_3Se_2$ has been shown in Fig. S5† and their kinetic values has been listed in Table S4.† As can be seen in Table S4,† $(Co_{0.21}Ni_{0.25}Cu_{0.54})_3Se_2$ catalyst showed a more efficient OER activity than the best ternary selenide $(Co_{0.40}Cu_{0.60})_3Se_2$ by shifting the onset η and η (at 10 mA cm^{-2}) by 16 and 6 mV in cathodic direction. It can be concluded that the quaternary mixed-metal selenides yielded

a significant enhancement in OER catalytic activity in terms of both overpotential at 10 mA cm^{-2} and low Tafel slope. A detailed SEM image of the $(Co_{0.21}Ni_{0.25}Cu_{0.54})_3Se_2$ thin film has been shown in Fig. 5b which indicates that the surface morphology of the thin film was mainly composed of rice-like and even hydrangea-like nanostructures with a broad size distribution of 100–500 nm. Such nanostructured grains are highly advantageous for electrocatalytic activity since they provide large active surface area. X-ray photoelectron spectroscopy (XPS) was carried out to study the elemental composition of the $(Co_{0.21}Ni_{0.25}Cu_{0.54})_3Se_2$ thin film and the corresponding oxidation states as shown in Fig. 5c–f. Binding energies for all elements (Cu, Co, Ni and Se) were calibrated with respect to the reference XPS spectrum of C 1s (284.5 eV). In the spectrum of Cu 2p shown in Fig. 5c, the peaks at 931.3 and 951.1 eV of Cu 2p were assigned to Cu^+ $2p_{3/2}$ and Cu^+ $2p_{1/2}$ respectively, while those at 933.4 and 953.3 eV were attributed to Cu^{2+} $2p_{3/2}$ and Cu^{2+} $2p_{1/2}$ with its shakeup satellite peaks at 941.4 and 961.4 eV.[78] As can be seen in the Co 2p spectrum (shown in Fig. 5d), the peaks at 777.5 and 792.4 eV corresponded to Co^{3+} $2p_{3/2}$ and Co^{3+} $2p_{1/2}$, while those at 780.1 and 795.7 eV were referred to Co^{2+} $2p_{3/2}$ and Co^{2+} $2p_{1/2}$ with its shakeup satellite peaks at 784.3 and 801.3 eV.[31,37] Similarly, the Ni 2p XPS spectrum in Fig. 5e showed peaks at 853.1 and 873.2 eV assigning to Ni^{2+} $2p_{3/2}$ and Ni^{2+} $2p_{1/2}$ and peaks at 855.7 and 874.1 eV assigning to Ni^{3+} $2p_{3/2}$ and Ni^{3+} $2p_{1/2}$, respectively, while the satellite peaks can be observed at 856.0 and 874.1 eV.[53,57] Fig. 5f showed the Se 3d spectrum where the peaks of $3d_{5/2}$ and $3d_{3/2}$ at the binding energies of 54.6 and 55.4 eV confirmed the presence of Se^{2-} and the peak around 59 eV indicated the existence of SeO_x which might be from the surface oxidation of selenide as reported by previous work.[79–81] It can be observed that the presence of mixed-valence metal ions in the deconvoluted spectra of Cu 2p, Co 2p and Ni 2p were all characterized as the selenide phases.

The electrochemically active surface area (ECSA) of the electrodeposited $(Co_{0.21}Ni_{0.25}Cu_{0.54})_3Se_2$ thin film was calculated from the double layer capacitance (C_{DL}) measurement. Specifically, cyclic voltammograms (CVs) of $(Co_{0.21}Ni_{0.25}Cu_{0.54})_3Se_2$ were measured in the N_2-saturated 1.0 M KOH from -0.28 to -0.33 V $vs.$ Ag|AgCl (KCl saturated) at various scan rates between 2.5 and 20 mV s^{-1} as shown in Fig. 6. The cathodic and anodic current was measured at -0.30 V $vs.$ Ag|AgCl (KCl saturated) (Fig. 6) and plotted as a function of scan rates as shown the inset of Fig. 6. C_{DL} can be obtained by averaging the cathodic and anodic slopes. The value of ECSA for $(Co_{0.21}Ni_{0.25}Cu_{0.54})_3Se_2$ catalyst was calculated by eqn (4). $(Co_{0.21}Ni_{0.25}Cu_{0.54})_3Se_2$ showed a relatively high ECSA of 3.68 cm^2 and high roughness factor of 52.57 confirming the highly textured granular surface of the catalysts as shown in the SEM images in Fig. 5b. It should be mentioned that the catalytic activity is expected to be improved by increasing roughness of the catalyst surface due to a more extensive exposure of the catalytically active sites to the electrolyte.

The faradaic efficiency of electrodeposited $(Co_{0.21}Ni_{0.25}Cu_{0.54})_3Se_2$ thin film for OER was evaluated by the water-displacement method, and the theoretical amount of evolved
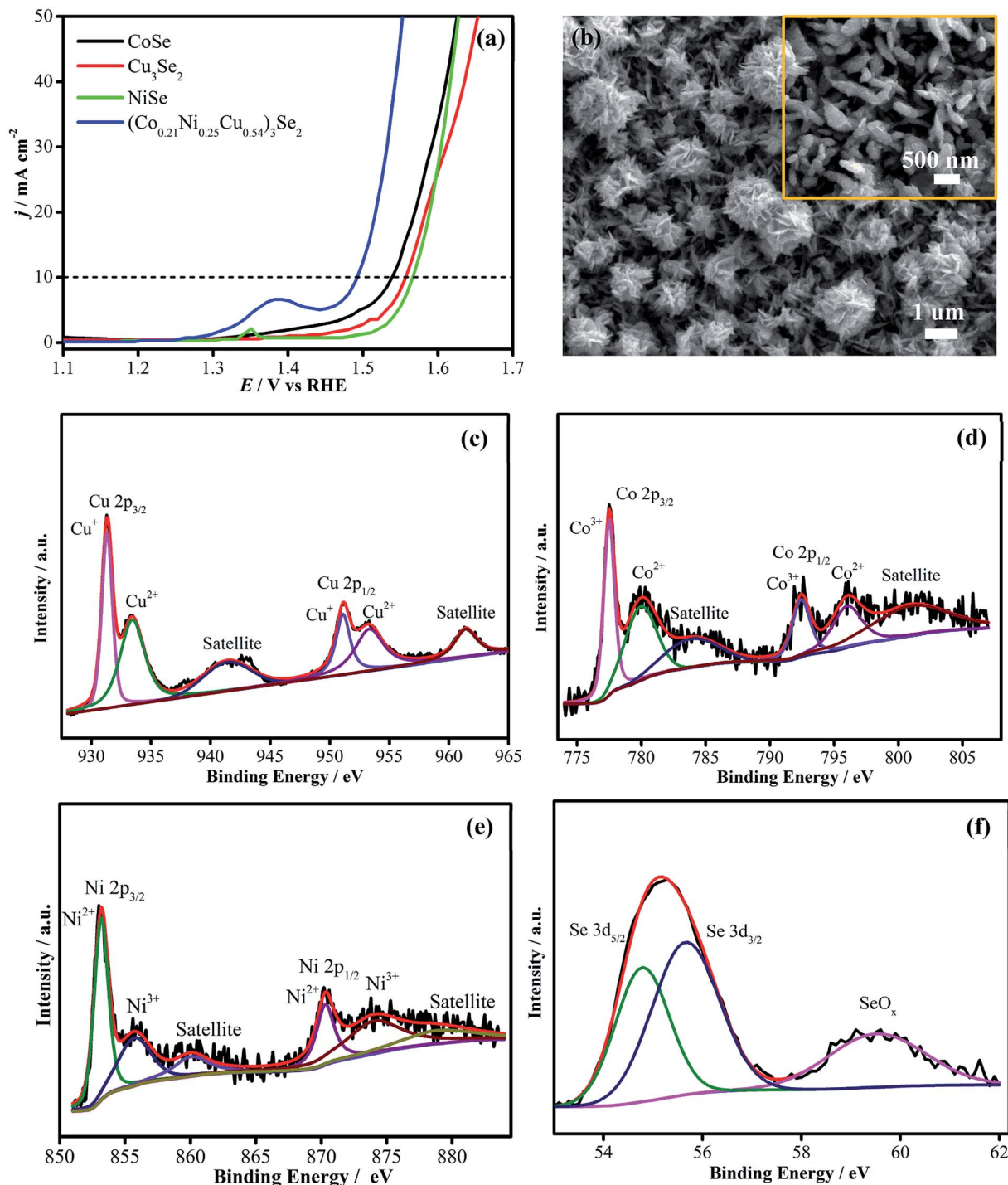
Fig. 5 (a) Polarization curves of $(Co_{0.21}Ni_{0.25}Cu_{0.54})_3Se_2$ in comparison to the binary selenide films. (b) SEM image of $(Co_{0.21}Ni_{0.25}Cu_{0.54})_3Se_2$ film and the inset is a higher magnification image. Deconvoluted XPS spectra of the as-deposited film $(Co_{0.21}Ni_{0.25}Cu_{0.54})_3Se_2$: (c) Cu $2p_{1/2}$ and $2p_{3/2}$ peaks; (d) Co $2p_{3/2}$ and $2p_{1/2}$ peaks; (e) Ni $2p_{3/2}$ and $2p_{1/2}$ peaks; (f) Se $3d_{5/2}$ and $3d_{3/2}$ peaks.

O_2 was compared with the experimentally measured O_2 as shown in Fig. 7. Nearly 100% Faradaic efficiency was observed, demonstrating superior catalytic efficiency of the $(Co_{0.21}Ni_{0.25}Cu_{0.54})_3Se_2$ catalyst for OER.

To further study the effect of mixed metal composition on the intrinsic property of the materials such as charge transport and conductivity which influences OER catalytic activity,

electrochemical impedance spectroscopy (EIS) was performed. From the EIS data, the internal resistance of thin films and charge-transfer resistance at the electrode and electrolyte interface was estimated which are the two parameters that influence the kinetic efficiency of an OER electrocatalyst. Therefore, the Nyquist plot of the best quaternary $(Co_{0.21}Ni_{0.25}Cu_{0.54})_3Se_2$ composition was compared with those of three
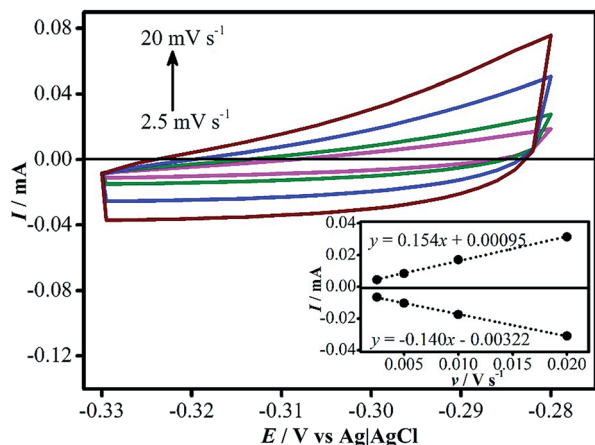
9884 | *J. Mater. Chem. A*, 2019, **7**, 9877–9889

This journal is © The Royal Society of Chemistry 2019

Fig. 6 Cyclic voltammograms measured for the $(Co_{0.21}Ni_{0.25}Cu_{0.54})_3Se_2$ thin film in N_2-saturated 1.0 M KOH solution at different scan rates from 2.5 to 20 mV s^{-1}. The inset is a plot of both anodic and cathodic currents measured at -0.30 V vs. Ag|AgCl (KCl saturated) as a function of scan rate.
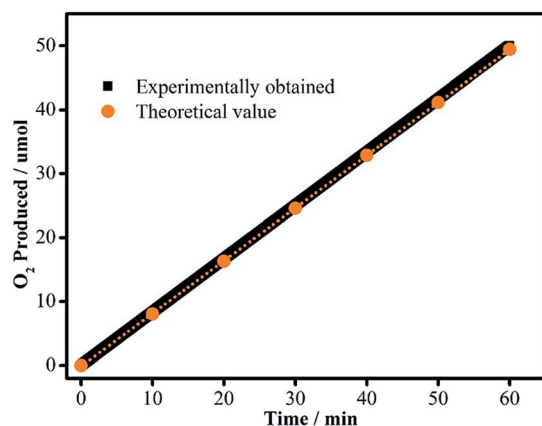

Fig. 7 The amount of theoretically calculated (black dots) oxygen and experimentally measured (red dots) oxygen of $(Co_{0.21}Ni_{0.25}Cu_{0.54})_3Se_2$ versus time at 0.7 V vs. Ag|AgCl (KCl saturated).

Fig. 8 Nyquist plots obtained from EIS measurements of CoSe, Cu_3Se_2, NiSe and $(Co_{0.21}Ni_{0.25}Cu_{0.54})_3Se_2$ catalysts at an applied potential of 0.5 V vs. Ag|AgCl (KCl saturated) in N_2-saturated 1.0 M KOH solution. Symbols indicate the raw data, while solid lines represent the corresponding fit to equivalent circuit model. Inset shows the equivalent circuit of catalysts.

Table 1 Equivalent circuit parameters obtained from fitting of EIS experimental data[a]

Catalysts	R_s/Ω	R_{ct}/Ω	CPE_{dl}/F	R_f/Ω	CPE_f/F
$(Co_{0.21}Ni_{0.25}Cu_{0.54})_3Se_2$	4.9	11.2	0.26	147.3	0.81
CoSe	5.0	14.2	0.35	312.6	0.83
Cu_3Se_2	5.0	18.4	0.48	1021.8	0.87
NiSe	5.0	279.1	0.66	1297.0	0.91

[a] R_s is the resistance of the electrolyte; R_{ct} is the electron transfer resistance; CPE_{dl} is the constant phase element of double-layer non-ideal capacitance; R_f is resistance of the catalyst layer; and CPE_f is the capacitance.

binary compounds Cu_3Se_2, CoSe and NiSe as shown in Fig. 8. The Nyquist plots were collected in N_2-saturated 1.0 M KOH at an applied potential of 0.5 V vs. Ag|AgCl (KCl saturated). The Nyquist plots were fitted to an equivalent circuit as inserted in Fig. 8, comprising electrolyte resistance (R_s), electron charge transfer resistance at the electrode (catalyst)-electrolyte interface (R_{ct}), and film resistance (R_f), and these values has been given in Table 1. The high frequency region of the Nyquist plots has been magnified and shown in Fig. S6.† As can be seen in Table 1, the resistance of 1.0 M KOH was estimated to be 5.0 Ω, which is similar to the previous reports and was used for iR correction of all the LSV plots reported in this work.[37,57] From the fitting of the equivalent circuit, it can be observed that $(Co_{0.21}Ni_{0.25}Cu_{0.54})_3Se_2$ showed the smallest charge transfer resistance (R_{ct}) in comparison to Cu_3Se_2, CoSe and NiSe, suggesting that the charge transfer rate at the thin film–electrolyte interface of $(Co_{0.21}Ni_{0.25}Cu_{0.54})_3Se_2$ was kinetically faster than
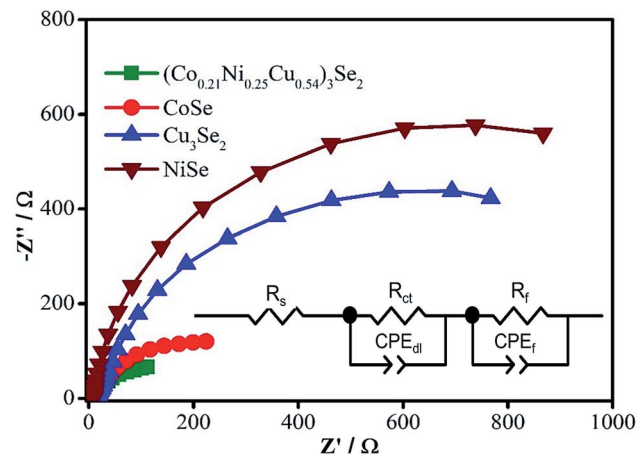
binary selenides. Such faster interfacial charge transfer at the electrocatalyst surface can facilitate the rate of the formation of intermediates on the surface and therefore decrease the OER onset potential resulting in a high catalytic efficiency of $(Co_{0.21}Ni_{0.25}Cu_{0.54})_3Se_2$.[69,82,83] Similarly, the film resistance (R_f) can also influence the overpotential at 10 mA cm^{-2} by facilitating charge transfer within the catalytic film, hence affecting the catalytic activity. It can be seen that $(Co_{0.21}Ni_{0.25}Cu_{0.54})_3Se_2$ exhibited a lower R_f value compared to that of three binaries shown in Table 1, suggesting the thin film showed a superior conductivity. The reduction in film resistance can be correlated with the increase in intrinsic conductivity with the incorporation of Cu atoms in the lattice. Overall, the enhancement of the OER activity of $(Co_{0.21}Ni_{0.25}Cu_{0.54})_3Se_2$ can be attributed to the improved charge transfer resistance at the electrode–electrolyte interface, and thin film resistance with transition metal doping within the catalyst composite. Ni and Co dopants into Cu_3Se_2 can lead to redistribution of the electron density around the catalytically active center in $(Co_{0.21}Ni_{0.25}Cu_{0.54})_3Se_2$, which can improve surface structure and optimize the bond strengths between the catalyst surface and intermediate adsorbates.

This journal is © The Royal Society of Chemistry 2019

J. Mater. Chem. A, 2019, 7, 9877–9889 | 9885

The stability and durability of the $(Co_{0.21}Ni_{0.25}Cu_{0.54})_3Se_2$ catalyst is an important parameter to evaluate its practical application and hence the catalytic film was studied under constant oxygen evolution for an extended period of time. Chronoamperometric measurement was performed for 12 h in N_2-saturated 1.0 M KOH solution at a constant applied potential of 1.505 V $vs.$ RHE to reach a current density of 10 mA cm^{-2} as shown in the inset of Fig. 9a. It was observed that large amount

of O_2 bubbles were continuously produced at the electrode surface during the chronoamperometric study. As can be seen, the $(Co_{0.21}Ni_{0.25}Cu_{0.54})_3Se_2$ catalyst exhibited an exceptional stability of the OER catalytic activity for over 12 h in 1.0 M KOH and the current density was even slightly improved. The LSV curves before and after the catalytic activity were also compared to further confirm the catalyst stability and are shown in Fig. 9a. As expected, the overpotential at 10 mA cm^{-2} was increased by
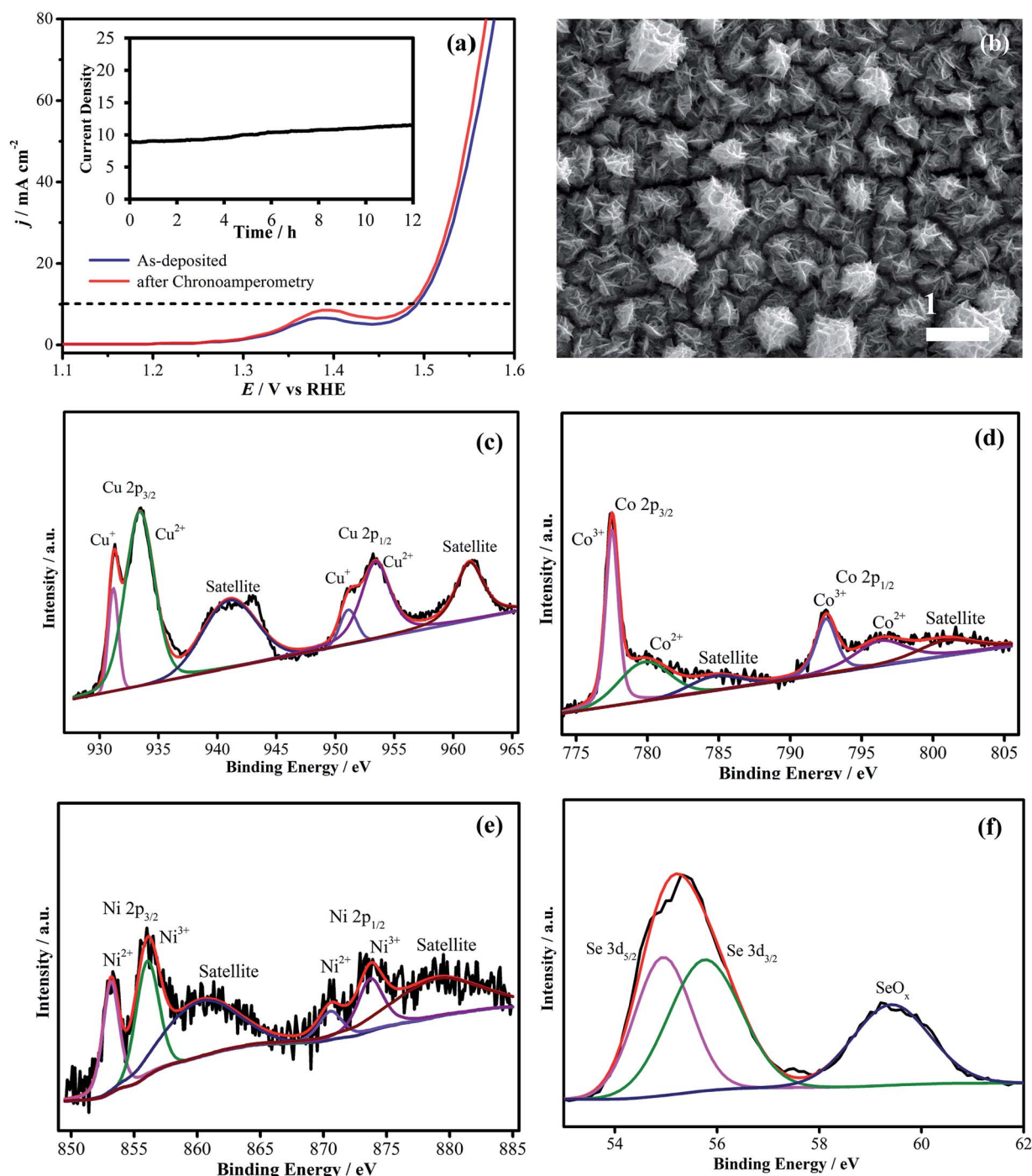

Fig. 9 (a) Comparison of LSVs before and after 12 h in N_2-saturated 1.0 M KOH solution. The inset is the chronoamperometry plot of $(Co_{0.21}Ni_{0.25}Cu_{0.54})_3Se_2$ for 12 h at an applied potential of 1.505 V $vs.$ RHE. (b) SEM image of $(Co_{0.21}Ni_{0.25}Cu_{0.54})_3Se_2$ after chronoamperometry (scale bar corresponds to 1 μm). (c–f) XPS spectra of $(Co_{0.21}Ni_{0.25}Cu_{0.54})_3Se_2$ after electrochemical measurement.

about 5 mV after chronoamperometry while the onset potential was almost the same. The activity enhancement can be attributed to the increased surface roughness of catalyst after 12 h of chronoamperometry shown in Fig. 9b. As can be seen from the SEM image, the surface morphology showed some changes mainly by creating lots of porous cracks on the surface which is believed to be due to the O_2 gas being evolved from the catalyst surface. These cracks can further facilitate electrolyte access to the catalytic site and facilitate catalyst activation through hydroxyl attachment on the catalytic site. The increase of surface roughness after prolonged catalytic activity has been further confirmed by measuring the ECSA of $(Co_{0.21}Ni_{0.25}Cu_{0.54})_3Se_2$ after chronoamperometry for 12 h as shown in Fig. S7.† On comparing the ECSA and roughness factor of the film before and after chronoamperometry, it was observed that both ECSA and RF showed a significant increase after catalytic activity, as shown in Table S5.† Such increase in surface roughness can be attributed to the evolution of large quantities of O_2 from the surface which makes it porous. The crystalline structure of the film after 12 h of chronoamperometry was also studied through pxrd. Fig. S8† shows the comparison of the pxrd patterns of $(Co_{0.21}Ni_{0.25}Cu_{0.54})_3Se_2$ before and after chronoamperometry. As can be seen from Fig. S8,† the diffraction pattern looks similar with slightly reduced peak intensities, confirming the structural stability of the catalyst during the prolonged period of catalytic activity. Compositional stability of the $(Co_{0.21}Ni_{0.25}Cu_{0.54})_3Se_2$ catalyst after prolonged OER activity was also confirmed by the XPS spectra shown in Fig. 9c–f which showed that the catalyst was still primarily composed of Cu, Ni, Co and Se with no trace of oxygen. The comparison of XPS spectra for, Cu 2p, Ni 2p, Co 2p and Se 3d in before and after chronoamperometry has been shown in Fig. S9.† The O 1s XPS spectra was also measured before and after chronoamperometry as shown in Fig. S10.† Analysis of the deconvoluted O 1s spectra revealed that there was chemisorbed oxygen species on the surface. However, there was no evidence of metal-bound oxygen (*i.e.* metal oxides), even after 12 h of chronoamperometry although some SeO_x was detected on the catalyst surface, corroborating well with the Se XPS spectra before and after activity. The XPS spectra along with EDS (shown in Table S6†) of $(Co_{0.21}Ni_{0.25}Cu_{0.54})_3Se_2$ before and after chronoamperometry further demonstrated the compositional stability of the catalyst. These studies confirmed that this OER electrocatalyst was both functionally durable and compositionally stable even after a long period of continuous O_2 evolution in alkaline medium.

It is interesting to note that while Ni and Co-selenide deposited as the mono-selenide phases, copper selenide crystallized as Cu_3Se_2, and the quaternary phases showed composition similar to M_3Se_2, indicating that Cu_3Se_2 structure type probably had a better stability under the reaction conditions and the quaternary phases were formed by substituting Cu with Ni and Co. It was also interesting to note that while Ni substitution in Cu_3Se_2 improved the catalytic activity, Cu substitution in NiSe did not exhibit similar improving trend. A comparison of the crystal structures of NiSe and Cu_3Se_2 (Fig. S11†) revealed that while NiSe contains octahedrally coordinated Ni atoms, Cu_3Se_2 was built by edge-shared and corner-shared $CuSe_4$

tetrahedral units. When Cu atoms are substituted with Ni and Co in the quaternary compositions, $[(Co_xNi_yCu_z)_3Se_2]$, it is expected that Ni and Co will also have tetrahedral coordination. Having lower coordination number at the catalytic site might be beneficial for initiation of catalytic activity which typically occurs *via* surface hydroxyl attachment. Low coordination of the catalytic site may facilitate the initiation step which can occur by coordination expansion without the need for anion displacement. In NiSe on the other hand, all the catalytically active transition metal sites are in octahedral coordination. Having an octahedral coordination of the catalytic site, makes the initiation step more challenging since the hydroxyl attachment in the surface necessitates anion displacement and is more energy intensive as a result. Hence Ni in a tetrahedral site may exhibit better onset of catalytic activity compared to Ni in the octahedral site. This may be one of the reasons (Ni,Co)-doped Cu_3Se_2 show significantly better catalytic activity than NiSe and Cu/Co-doped NiSe. The effect of structure type was also visible in the ternary selenides in the Ni–Co–Cu phase space. For the Co–Cu selenides, all the ternary films form the M_3Se_2 composition, and they can be described as Co-doped Cu_3Se_2. The Ni–Cu selenide group on the other hand, forms the MSe structure type and are closer to Cu doped NiSe systems. As explained above these stoichiometries are distinctly different from each other and contains different coordinations of the transition metal ions and such differences in coordination geometry may lead to different OER catalytic activity.

Conclusions

In summary, we have successfully screened the Co–Ni–Cu ternary phase space and shown that Co and Ni-doped copper selenide shows high efficiency for OER in alkaline medium surpassing that of the binary and ternary selenides within the same phase space. The series of mixed metal selenides were synthesized through combinatorial electrodeposition exploring the ternary Co–Ni–Cu phase diagram. Systematic investigation of the OER activity with respect to the composition showed that the quaternary selenides showed higher activity in comparison to ternaries and binaries. A slightly higher amount of Cu doping increased the catalytic activity, however, a very high concentration of Cu can produce negative effect for the activity. Higher activities were observed for quaternary selenides showing a Cu_3Se_2 crystal structure with slight change in lattice spacings due to Ni and Co doping. The optimal quaternary composition $(Co_{0.21}Ni_{0.25}Cu_{0.54})_3Se_2$ exhibited a superior catalytic activity with low onset overpotential of 241 mV and overpotential of 272 mV to achieve a current density of 10 mA cm^{-2} in N_2-saturated 1.0 M KOH. Specifically, with proper amount of Co and Ni introduced, $(Co_{0.21}Ni_{0.25}Cu_{0.54})_3Se_2$ showed enhanced catalytic activity with 54 mV lower overpotential than its parent Cu_3Se_2 (umangite) at 10 mA cm^{-2}. The concept that introduction of Cu can significantly improve the catalytic efficiencies of the transition metal selenides will be immensely useful for other catalyst systems with different crystal structures and stoichiometries.

This journal is © The Royal Society of Chemistry 2019

J. Mater. Chem. A, 2019, **7**, 9877–9889 | **9887**

Conflicts of interest

The authors declare no conflict of interest.

Acknowledgements

Notes and references

1 J. Chow, R. J. Kopp and P. R. Portney, *Science*, 2009, **302**, 1528–1531.

2 N. S. Lewis, *Science*, 2007, **315**, 798–801.

3 M. G. Walter, E. L. Warren, J. R. Mckone, S. W. Boettcher, Q. Mi, E. A. Santori and N. S. Lewis, *Chem. Rev.*, 2010, **110**, 6446–6473.

4 J. A. Turner, *Science*, 2004, **305**, 972–974.

5 M. S. Dresselhaus and I. L. Thomas, *Nature*, 2001, **414**, 332–337.

6 G. W. Crabtree, M. S. Dresselhaus and M. V. Buchanan, *Phys. Today*, 2004, **57**, 39–44.

7 N. T. Suen, S. F. Hung, Q. Quan, N. Zhang, Y. J. Xu and H. M. Chen, *Chem. Soc. Rev.*, 2017, **46**, 337–365.

8 H. Dau, C. Limberg, T. Reier, M. Risch, S. Roggan and P. Strasser, *ChemCatChem*, 2010, **2**, 724–761.

9 M. T. M. Koper, *J. Electroanal. Chem.*, 2011, **660**, 254–260.

10 J. Rossmeisl, A. Logadottir and J. K. Nørskov, *Chem. Phys.*, 2005, **319**, 178–184.

11 T. Reier, M. Oezaslan and P. Strasser, *ACS Catal.*, 2012, **2**, 1765–1772.

12 W. T. Hong, M. Risch, K. A. Stoerzinger, A. Grimaud, J. Suntivich and Y. Shao-Horn, *Energy Environ. Sci.*, 2015, **8**, 1404–1427.

13 M. Gong and H. Dai, *Nano Res.*, 2015, **8**, 23–39.

14 L. Yang, S. Jiang, Y. Zhao, L. Zhu, S. Chen, X. Wang, Q. Wu, J. Ma, Y. Ma and Z. Hu, *Angew. Chem., Int. Ed.*, 2011, **50**, 7132–7135.

15 Y. Lee, J. Suntivich, K. J. May, E. E. Perry and Y. Shao-Horn, *J. Phys. Chem. Lett.*, 2012, **3**, 399–404.

16 H. Over, *Chem. Rev.*, 2012, **112**, 3356–3426.

17 Y. Li, P. Hasin and Y. Wu, *Adv. Mater.*, 2010, **22**, 1926–1929.

18 F. Dionigi and P. Strasser, *Adv. Energy Mater.*, 2016, **6**, 1600621.

19 R. Subbaraman, D. Tripkovic, K. C. Chang, D. Strmcnik, A. P. Paulikas, P. Hirunsit, M. Chan, J. Greeley, V. Stamenkovic and N. M. Markovic, *Nat. Mater.*, 2012, **11**, 550–557.

20 H. Osgood, S. V. Devaguptapu, H. Xu, J. Cho and G. Wu, *Nano Today*, 2016, **11**, 601–625.

21 M. Gong, Y. Li, H. Wang, Y. Liang, J. Z. Wu, J. Zhou, J. Wang, T. Regier, F. Wei and H. Dai, *J. Am. Chem. Soc.*, 2013, **135**, 8452–8455.

22 A. Kargar, S. Yavuz, T. K. Kim, C. H. Liu, C. Kuru, C. S. Rustomji, S. Jin and P. R. Bandaru, *ACS Appl. Mater. Interfaces*, 2015, **7**, 17851–17856.

23 Q. Chen and J. A. Switzer, *ACS Appl. Mater. Interfaces*, 2018, **10**, 21365–21371.

24 T. Maiyalagan, K. A. Jarvis, S. Therese, P. J. Ferreira and A. Manthiram, *Nat. Commun.*, 2014, **5**, 3949.

25 J. Suntivich, K. J. May, H. A. Gasteiger, J. B. Goodenough and Y. Shao-Horn, *Science*, 2011, **334**, 1383–1385.

26 A. Grimaud, K. J. May, C. E. Carlton, Y. L. Lee, M. Risch, W. T. Hong, J. Zhou and Y. Shao-Horn, *Nat. Commun.*, 2013, **4**, 2439.

27 X. Long, J. Li, S. Xiao, K. Yan, Z. Wang, H. Chen and S. Yang, *Angew. Chem., Int. Ed.*, 2014, **53**, 7584–7588.

28 U. De Silva, J. Masud, N. Zhang, Y. Hong, W. P. R. Liyanage, M. Asle Zaeem and M. Nath, *J. Mater. Chem. A*, 2018, **6**, 7608–7622.

29 M. Shen, C. Ruan, Y. Chen, C. Jiang, K. Ai and L. Lu, *ACS Appl. Mater. Interfaces*, 2015, **7**, 1207–1218.

30 Q. Liu, J. Jin and J. Zhang, *ACS Appl. Mater. Interfaces*, 2013, **5**, 5002–5008.

31 P. Ganesan, M. Prabu, J. Sanetuntikul and S. Shanmugam, *ACS Catal.*, 2015, **5**, 3625–3637.

32 J. Chang, Y. Xiao, M. Xiao, J. Ge, C. Liu and W. Xing, *ACS Catal.*, 2015, **5**, 6874–6878.

33 L. A. Stern, L. Feng, F. Song and X. Hu, *Energy Environ. Sci.*, 2015, **8**, 2347–2351.

34 P. He, X. Y. Yu and X. W. Lou, *Angew. Chem., Int. Ed.*, 2017, **56**, 3897–3900.

35 A. T. Swesi, J. Masud and M. Nath, *Energy Environ. Sci.*, 2016, **9**, 1771–1782.

36 X. Xu, F. Song and X. Hu, *Nat. Commun.*, 2016, **7**, 12324.

37 J. Masud, A. T. Swesi, W. P. R. Liyanage and M. Nath, *ACS Appl. Mater. Interfaces*, 2016, **8**, 17292–17302.

38 W. Li, X. Gao, D. Xiong, F. Wei, W. G. Song, J. Xu and L. Liu, *Adv. Energy Mater.*, 2017, **7**, 1602579.

39 S. C. Petitto, E. M. Marsh, G. A. Carson and M. A. Langell, *J. Mol. Catal. A: Chem.*, 2008, **281**, 49–58.

40 L. Zhuang, L. Ge, Y. Yang, M. Li, Y. Jia, X. Yao and Z. Zhu, *Adv. Mater.*, 2017, **29**, 1606793.

41 H. Y. Wang, Y. Y. Hsu, R. Chen, T. S. Chan, H. M. Chen and B. Liu, *Adv. Energy Mater.*, 2015, **5**, 1500091.

42 J. Landon, E. Demeter, N. Inoğlu, C. Keturakis, I. E. Wachs, R. Vasić, A. I. Frenkel and J. R. Kitchin, *ACS Catal.*, 2012, **2**, 1793–1801.

43 Y. C. Liu, J. A. Koza and J. A. Switzer, *Electrochim. Acta*, 2014, **140**, 359–365.

44 K. Xu, H. Ding, H. Lv, S. Tao, P. Chen, X. Wu, W. Chu, C. Wu and Y. Xie, *ACS Catal.*, 2017, **7**, 310–315.

45 G. Zhang, S. Zang, Z. A. Lan, C. Huang, G. Li and X. Wang, *J. Mater. Chem. A*, 2015, **3**, 17946–17950.

46 J. X. Feng, H. Xu, Y. T. Dong, S. H. Ye, Y. X. Tong and G. R. Li, *Angew. Chem., Int. Ed.*, 2016, **55**, 3694–3698.

47 S. Zou, M. S. Burke, M. G. Kast, J. Fan, N. Danilovic and S. W. Boettcher, *Chem. Mater.*, 2015, **27**, 8011–8020.

48 L. Han, X. Y. Yu and X. W. Lou, *Adv. Mater.*, 2016, **28**, 4601–4605.

9888 | *J. Mater. Chem. A*, 2019, **7**, 9877–9889

This journal is © The Royal Society of Chemistry 2019

49 M. Görlin, J. F. De Araujo, H. Schmies, D. Bernsmeier, S. Dresp, M. Gliech, Z. Jusys, P. Chernev, R. Kraehnert, H. Dau and P. Strasser, *J. Am. Chem. Soc.*, 2017, **139**, 2070–2082.

50 M. Görlin, P. Chernev, J. F. De Araújo, T. Reier, S. Dresp, B. Paul, R. Krähnert, H. Dau and P. Strasser, *J. Am. Chem. Soc.*, 2016, **138**, 5603–5614.

51 L. J. Enman, M. S. Burke, A. S. Batchellor and S. W. Boettcher, *ACS Catal.*, 2016, **6**, 2416–2423.

52 Y. Xu, W. Bian, J. Wu, J. H. Tian and R. Yang, *Electrochim. Acta*, 2015, **151**, 276–283.

53 Z. Wang, J. Li, X. Tian, X. Wang, Y. Yu, K. A. Owusu, L. He and L. Mai, *ACS Appl. Mater. Interfaces*, 2016, **8**, 19386–19392.

54 G. Liu, K. Wang, X. Gao, D. He and J. Li, *Electrochim. Acta*, 2016, **211**, 871–878.

55 R. D. L. Smith, M. S. Prévot, R. D. Fagan, S. Trudel and C. P. Berlinguette, *J. Am. Chem. Soc.*, 2013, **135**, 11580–11586.

56 A. Shinde, D. Guevarra, G. Liu, I. D. Sharp, F. M. Toma, J. M. Gregoire and J. A. Haber, *ACS Appl. Mater. Interfaces*, 2016, **8**, 23696–23705.

57 X. Cao, Y. Hong, N. Zhang, Q. Chen, J. Masud, M. A. Zaeem and M. Nath, *ACS Catal.*, 2018, **8**, 8273–8289.

58 Z. Chen and T. J. Meyer, *Angew. Chem., Int. Ed.*, 2013, **52**, 700–703.

59 M. T. Zhang, Z. Chen, P. Kang and T. J. Meyer, *J. Am. Chem. Soc.*, 2013, **135**, 2048–2051.

60 M. Qian, X. Liu, S. Cui, H. Jia and P. Du, *Electrochim. Acta*, 2018, **263**, 318–327.

61 Y. Liu, Z. Niu, Y. Lu, L. Zhang and K. Yan, *J. Alloys Compd.*, 2018, **735**, 654–659.

62 L. Yang, L. Xie, X. Ren, Z. Wang, Z. Liu, G. Du, A. M. Asiri, Y. Yao and X. Sun, *Chem. Commun.*, 2018, **54**, 78–81.

63 X. Du, X. Zhang, Z. Xu, Z. Yang and Y. Gong, *Int. J. Hydrogen Energy*, 2018, **43**, 5012–5018.

64 P. Zhang, L. Li, D. Nordlund, H. Chen, L. Fan, B. Zhang, X. Sheng, Q. Daniel and L. Sun, *Nat. Commun.*, 2018, **9**, 381.

65 J. Masud, W. P. R. Liyanage, X. Cao, A. Saxena and M. Nath, *ACS Appl. Energy Mater.*, 2018, **1**, 4075–4083.

66 C. C. L. Mccrory, S. Jung, J. C. Peters and T. F. Jaramillo, *J. Am. Chem. Soc.*, 2013, **135**, 16977–16987.

67 C. C. L. McCrory, S. Jung, I. M. Ferrer, S. M. Chatman, J. C. Peters and T. F. Jaramillo, *J. Am. Chem. Soc.*, 2015, **137**, 4347–4357.

68 L. Trotochaud, S. L. Young, J. K. Ranney and S. W. Boettcher, *J. Am. Chem. Soc.*, 2014, **136**, 6744–6753.

69 M. S. Burke, M. G. Kast, L. Trotochaud, A. M. Smith and S. W. Boettcher, *J. Am. Chem. Soc.*, 2015, **137**, 3638–3648.

70 M. K. Bates, Q. Jia, H. Doan, W. Liang and S. Mukerjee, *ACS Catal.*, 2016, **6**, 155–161.

71 L. J. Enman, M. S. Burke, A. S. Batchellor and S. W. Boettcher, *ACS Catal.*, 2016, **6**, 2416–2423.

72 X. Xu, F. Song and X. Hu, *Nat. Commun.*, 2016, **7**, 12324.

73 J. Deng, M. R. Nellist, M. B. Stevens, C. Dette, Y. Wang and S. W. Boettcher, *Nano Lett.*, 2017, **17**, 6922–6926.

74 A. S. Batchellor, G. Kwon, F. A. L. Laskowski, D. M. Tiede and S. W. Boettcher, *J. Phys. Chem. C*, 2017, **121**, 25421–25429.

75 Y. Liang, Y. Li, H. Wang, J. Zhou, J. Wang, T. Regier and H. Dai, *Nat. Mater.*, 2011, **10**, 780–786.

76 L. R. B. Elton and D. F. Jackson, *Am. J. Phys.*, 1966, **34**, 1036–1038.

77 U. Holzwarth and N. Gibson, *Nat. Nanotechnol.*, 2011, **6**, 534.

78 M. Chauhan, K. P. Reddy, C. S. Gopinath and S. Deka, *ACS Catal.*, 2017, **7**, 5871–5879.

79 A. Panneerselvam, M. A. Malik, M. Afzaal, P. O'Brien and M. Helliwell, *J. Am. Chem. Soc.*, 2008, **130**, 2420–2421.

80 W. Wang, Y. Geng, P. Yan, F. Liu, Y. Xie and Y. Qian, *J. Am. Chem. Soc.*, 1999, **121**, 4062–4063.

81 J. Nai, Y. Lu, L. Yu, X. Wang and X. W. D. Lou, *Adv. Mater.*, 2017, **29**, 1703870.

82 P. Liao, J. A. Keith and E. A. Carter, *J. Am. Chem. Soc.*, 2012, **134**, 13296–13309.

83 N. B. Halck, V. Petrykin, P. Krtil and J. Rossmeisl, *Phys. Chem. Chem. Phys.*, 2014, **16**, 13682–13688.